Novel Balloon Surface Scanning Device for Intraoperative Breast Endomicroscopy.

Siyang Zuo, Michael Hughes, Guang-Zhong Yang

Institutions: Imperial College London

Published on: 01 Jul 2016 - Annals of Biomedical Engineering (Ann Biomed Eng)

Topics: Endomicroscopy

Title page

Novel Balloon Surface Scanning Device for Intraoperative Breast Endomicroscopy

Siyang Zuo, Michael Hughes, and Guang-Zhong Yang

Hamlyn Centre for Robotic Surgery, Imperial College London, London SW7 2AZ, U.K.

Tel: +44 (0) 20 7594 0814

Fax:+44 (0)20 7594 8260

E-mail: siyang.zuo@gmail.com

Abstract

Recent advances in fluorescence confocal endomicroscopy have allowed real-time identification of residual tumour cells on the walls of the cavity left by breast conserving surgery. However, it is difficult to systematically survey the surgical site because of the small imaging field-of-view of these probes, compounded by tissue deformation and inconsistent probe-tissue contact when operated manually. Therefore, a new robotized scanning device is required for controlled, large area scanning and mosaicing.This paper presents a robotic scanning probe with an inflatable balloon, providing stable cavity scanning over undulating surfaces. It has a compact design, with an outer diameter of 4 mm and a working channel of 2.2 mm, suitable for a leached flexible fibre bundle endomicroscope probe. With the probe inserted, the tip positioning accuracy measured to be 0.26 mm for bending and 0.17 mm for rotational motions. Large area scanning was achieved (25-35 mm^2) and the experimental results demonstrate the potential clinical value of the device for intraoperative cavity tumour margin evaluation.

Keywords: Breast conserving surgery, confocal endomicroscopy, image mosaicing, mechanical design, surgical robot

INTRODUCTION

Breast cancer is the second most common cancer in the world and, by far the most frequent cancer among women with an estimated 1.67 million new cancer cases diagnosed in 2012 (11.9% of all cancers) [1]. Breast conserving surgery (BCS) is a procedure for treating smaller cancers by removing the tumour and a part of normal tissue while sparing the remainder of the breast [2]. However, complete tumour removal is currently confirmed post-operatively by histology, which often results in patient being required to return to theatre for further surgery [3]. A re-operation has several disadvantages, including risks of infections, poor cosmesis, and higher costs. [4].

Photoacoustic microscopy using focused lasers with ultrasound transducers as receivers have been shown to have the ability to create sub-micron resolution images of cells and tissue [5]. Furthermore, fluorescence confocal endomicroscopy[6]has been developed to image and diagnose cancer *in situ* [7-11], particularly in the gastro-intestinal tract. It can obtain optically sectioned, high-resolution images of tissue *in situ*, which has previously been stained using a fluorescent agent such fluorescein or acriflavine. It involves use of a miniaturized microscope probe, inserted through the instrument channel of an endoscope or similar device, and placed in direct contact with the tissue. Given the difficulties of miniaturizing the device for the high-speed laser scanning needed for confocal imaging, a common approach is to relay light to and from the tissue using a fibre imaging bundle [12-14]. This allows the entire optical system to be positioned outside the patient.

More recently, it has been suggested that endomicroscopy could be adapted to intraoperative imaging of breast tissue [15-16]. For this application, the probe would be inserted into the cavity created by removal of the tumour and used to search for residual tumour cells on the cavity wall. Bench-top confocal endomicroscopy has already been considered for analysis of breast tissues, and been shown to allow key morphological structures of normal and cancerous breast tissues to be identified and differentiated [17]. By offering a way to identify the margins of the tumour*in situ,*endomicroscopy could therefore reduce the currently high rates of reoperations [18], as well as reducing high cancer recurrence rates due to incomplete excision.

However, endomicroscopy has several limitations that have made breast imaging challenging. Most importantly, the limited number of fibre cores in the fibre bundle means that only a small field-of-view can be obtained (typically less than 0.5 mm for high resolution probes). Video mosaicing techniques can be used to mitigate this problem [19-21], but scanning over large areas is time-consuming and requires high dexterity. Mechanical scanning of the probe has therefore been proposed for laparoscopic applications, including a scanning device using hydraulic micro-balloons [22], and a conic screw-like structure [23]. However, the area imaged by the miniaturised versions of these designs is typically less than 3 mm^2.

Many existing robotic devices, including the da Vinci robot (Intuitive Surgical), utilize wire-driven mechanisms to transfer actuation power from actuators to actuated parts in the tip of the forceps [24-26]. While the wire driven mechanism allows miniaturization of multi Degree of Freedom (DOF) structures, problems of friction, wearing and extension are practical difficulties to consider. Alternatively, some manipulators are driven by linkage mechanisms [27-29]. They provide a high stiffness, durability, and strong force. However, the reported linkage driven mechanisms often result in an increase in the number of parts. Furthermore, it is particularly difficult to reduce the backlash when there is a large number of linkages.

A preliminary prototype of a breast scanning device, using a rigid concentric tubes scanning mechanism, has previously been reported [30]. However, the outer diameter of the device was 6 mm, which is large for this application. The device was demonstrated using a fibre bundle probe taken from a Cellvizioendomicroscope (Mauna Kea Technologies), which had limited flexibility, restricting the scan area.There were also difficulties with tissue deformation as the probe was scanned across the tissue.

In this study, we propose a new device which uses a gear-guided linkage scanning mechanism to enable safe, efficient and accurate large area scanning of the breast cavity. This scanning device would be inserted through the incision created during BCS, and deployed against the cavity walls, thus allowing high quality image mosaics to be created (Fig. 1). The scanning is performed inside an inflatable balloon which could help to stabilize the tissue by pressing the balloon on it. A custom-built probe, using a leached fibre bundle and a micro-lens, allows the full range of motion of the device to be used and provides sufficient working distance to allow imaging through the balloon. The mechanical characteristics of the device are analyzed, and imaging results from a breast phantom and *ex vivo* human breast tissue are presented, showing that the device can achieve large area endomicroscopy imaging and mosaicing.

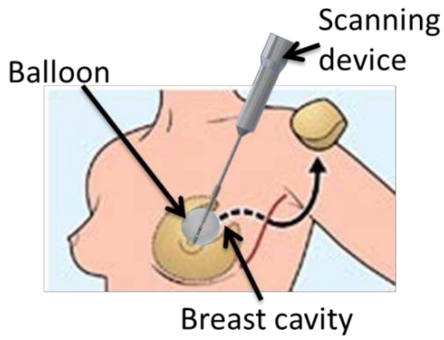

FIGURE 1.Concept of the breast scanning system with an inflated balloon during breast conserving surgery for breast cancer.

MATERIALS AND METHODS

Scanning Mechanism

To achieve both a small outer diameter and a large inner diameter for the device, the design concept needed to be simple and with a small number of parts. The proposed device has the ability to scan over an arbitrary trajectory by combining bending and rotational motion of the tip. The scanning structure, illustrated in Fig. 2, is based on an epicyclic motion between the tip and base frames. The tip frame and base frame are in contact with spur gears and are connected by the middle frame. Bending motion is driven by linear movement of the linkage, and rotational motion is provided by rotation of the base frame. This provides 0 to +90 degrees bending on one axis, and 360 degrees of rotation on the second axis. The tip frame and base frame are guided by spur gears, which enable smooth bending motion without slippage (tip bending repeatability of 0.6 degrees as shown in RESULTS section)between the frames.

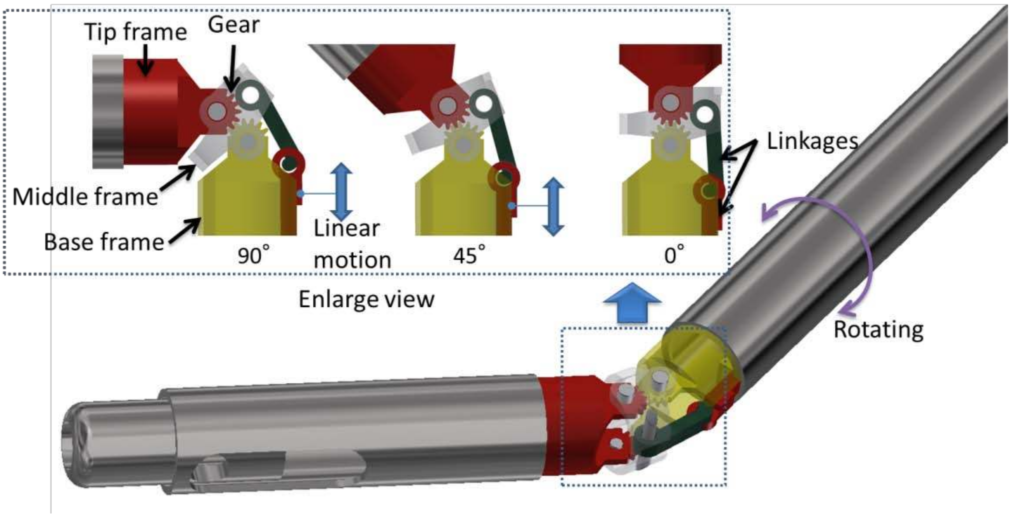

FIGURE 2.The configuration of the scanning mechanism, transforming linear motion of the linkages and rotational motion of the base frame to a 2D scanning motion of the tip.

Miniature Scanning Device

The scanning prototype is 4 mm in diameter, incorporating a central hollow channel (2.2 mm in diameter), through which the endomicroscope probe can be deployed, as shown in Fig. 3(a). The device has a length of 95 mm, while the bending tip has a length of 25 mm. The scanning structure was fabricated from stainless steel. A passive linear structure is located at the distal end (Fig. 3(b)), consisting of a slider, a spring and a slide guiding tube. The endomicroscope probe is fixed on the linear structure, helping to ensure consistent contact between the tip and the tissue (Fig. 3(b)).The endomicroscope probe can easily be separated from this structure for cleaning. The workspace of the scanning device’s tip is a large hemisphere, as shown in Fig. 3 (e).

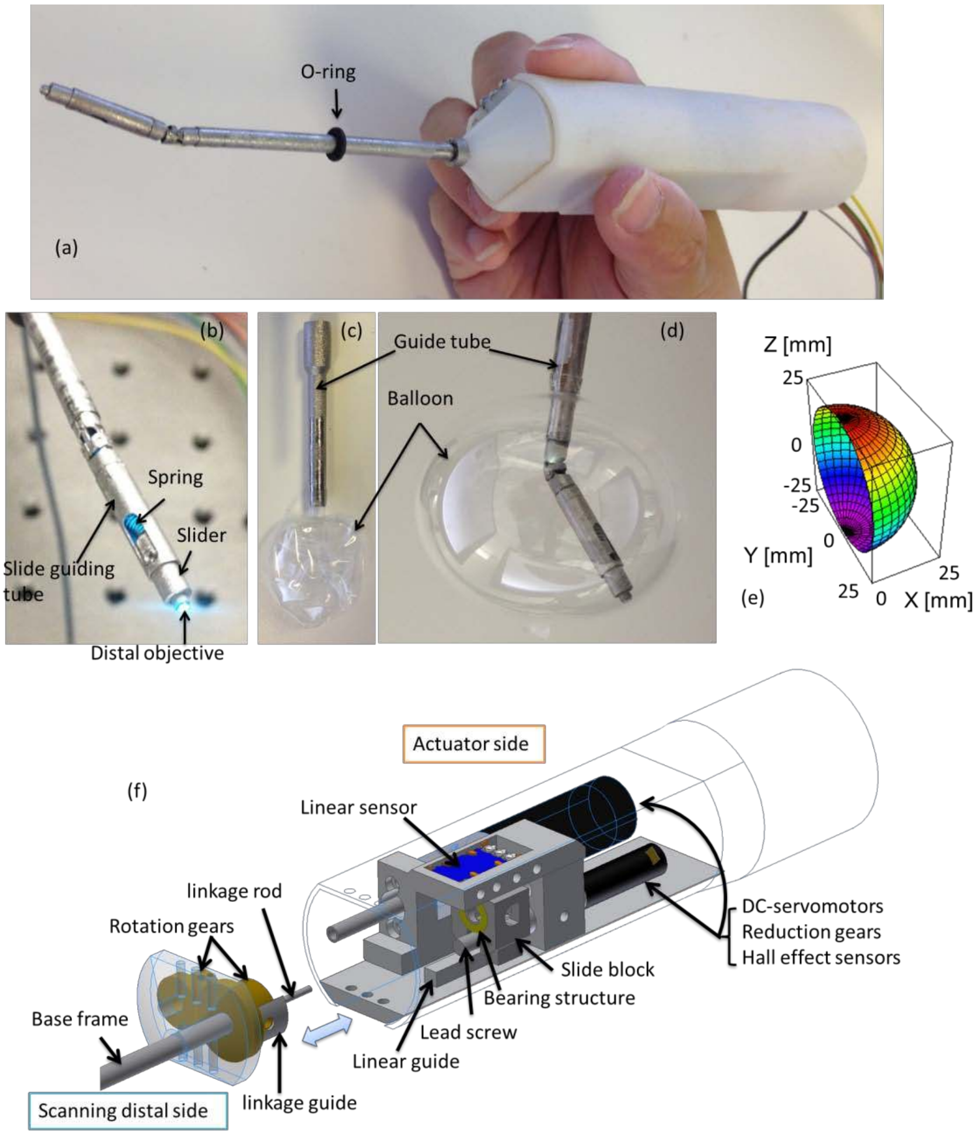

FIGURE 3 A prototype of the scanning device, showing (a) the image of scanner, (b) distal end with distal object, (c) Balloon with guide tube, (d) distal end with balloon inflation, (e) The workspace of the scanning device's tip with motorized bending and rotating motions. The workspace of the tip is a large hemi-sphere. (f) Details of the drive unit to drive 2-DOFs scanning mechanism.

The base frame is driven by a high-resolution brushless DC-servomotor equipped with a gear head and Hall effect sensor (1226 E 012 B K1855, Faulhaber SA, Germany) (Fig. 3(f)). The unit driving the linear motion of the linkage consists of a lead screw, a brushless DC-servomotor (0620 C 012 B K1855, Faulhaber SA, Germany), a linear position sensor (EVA-W7XR04B34, Panasonic, Japan), a linkage guide and a bearing slide block (Fig. 3(f)). The linkage rod is fixed to the bearing structure which rotates with the base frame, thus providing simultaneous linear and rotational motions. The drive unit is enclosed within in a cylindrical cover with outer diameter less than 30 mm,and the total weight of the scanning device is 83 g, thus making it suitable for handheld use. For cleaning and sterilization purposes, the scanning distal side can easily be separated from the driver unit. A standard computer calculates rotational and linear displacements of the base frame and linkage from inputted target values.

Tip Scanning Balloon

A balloon inflation system was developed to provide a smooth scan surface and minimize tissue deformation. The balloon is a commercial medical balloon(Model: 30000000BC, material: Urethane Very Low Durometer, Vention Medical, USA) with an inflated diameter of 30-50 mm and aninflated wall thickness of 15- 20μm(Fig. 3(c-d)). The balloon is fixed on a guide tube, and the scanning device is inserted into the guide tube (5 mm in outer diameter) during scanning (Fig. 3(c-d)). An O-ring is used to seal the cap between guide tube and scanning device, and there is an inner spacer inserted into the working channel to prevent an air leakage. The scanning device is connected to a micro diaphragm air pump (8018Gt, Namiki Precision Jewel Co., Ltd, Japan), and the inner pressure of the balloon was detected by a pressure sensor (MLH150PSB01A, Honeywell). It was experimentally determined that stable scanning was obtained when maintaining an inner pressure of 140 kPa.

Kinematics, Control algorithm and Trajectory

We developed a custom user interface (Labview, National Instruments) to control the prototype from a standard PC. Once the scan parameters are entered, the device can scan the target surface automatically.

The relationship between the bending angle, θ, and linear linkage displacement, y, is given by (1), where the lengths a, b, and c are shown in Fig. 4 (a).

$$y = \mathrm{a} + \mathrm{b}\left(\cos\frac{\theta}{2} - 1\right) + c\sin\frac{\theta}{2} - \sqrt{a^2 - \left\{b\sin\frac{\theta}{2} + c(1 - \cos\frac{\theta}{2})\right\}^2}$$

$$= f\ (\theta, a, b, c) \qquad (1)$$

The inverse function $f^{-1}(\theta, a, b, c)$of (3) can be computed as follows:

$$a^2 - \left\{b\sin\frac{\theta}{2} + c(1 - \cos\frac{\theta}{2})\right\}^2 = \left\{\mathrm{a} + \mathrm{b}\left(\cos\frac{\theta}{2} - 1\right) + c\sin\frac{\theta}{2} - y\right\}^2$$

$$\{b^2 + c^2 + (y - a)b\}\cos\frac{\theta}{2} + (y - a)c\sin\frac{\theta}{2}$$

$$= b^2 + c^2 + (b - a)y + \frac{1}{2}y^2 - ba \qquad (2)$$

When,

$$A(y) = b^2 + c^2 + (y - a)b$$

$$B(y) = (y - a)c$$

$$C(y) = b^2 + c^2 + (b - a)y + \frac{1}{2}y^2 - ba$$

Then equation (2) can be converted to:

$$A(y)\cos\frac{\theta}{2} = C(y) - B(y)\sin\frac{\theta}{2}$$

$$\{A(y)^2 + B(y)^2\}\sin^2\frac{\theta}{2} - 2B(y)C(y)\sin\frac{\theta}{2} + \{C(y)^2 - A(y)^2\}(3)$$

When *A(y) = 0; y =* $\frac{1}{b}(ab - b^2 - c^2)$,

$$\theta = 2\arcsin\left\{\frac{C(y)}{B(y)}\right\} \qquad (4)$$

When $A(y) \neq 0$,

$$\sin\frac{\theta}{2} = \frac{B(y)C(y) \pm \sqrt{B(y)^2C(y)^2 - (A(y)^2 + B(y)^2)(C(y)^2 - A(y)^2)}}{A(y)^2 + B(y)^2} \qquad (5)$$

Combining (4) and (5), the complete expression for the bending angle θ can be given as follows:

$$\theta = \begin{cases} 2\arcsin\left\{\dfrac{B(y)C(y) - \sqrt{B(y)^2C(y)^2 - (A(y)^2 + B(y)^2)(C(y)^2 - A(y)^2)}}{A(y)^2 + B(y)^2}\right\} & (y < \frac{1}{b}(ab - b^2 - c^2) \\ 2\arcsin\left\{\dfrac{C(y)}{B(y)}\right\} (y = \frac{1}{b}(ab - b^2 - c^2)) & \\ 2\arcsin\left\{\dfrac{B(y)C(y) + \sqrt{B(y)^2C(y)^2 - (A(y)^2 + B(y)^2)(C(y)^2 - A(y)^2)}}{A(y)^2 + B(y)^2}\right\} & (y > \frac{1}{b}(ab - b^2 - c^2) \end{cases}$$

The relationship between linear linkage displacement, y, and bending angle, θ, is illustrated in Fig. 4 (b). For our prototype, where a = 2.9 mm, b = 1.14 mm, c = 1.3 mm, and 0 <θ < 90 degrees, y is given by:

$$y = \frac{W_{m1} \cdot t \cdot \Delta p}{\mu_1 \cdot 60} \tag{6}$$

where μ_1 is the gear reduction ratio of Motor 1 (which controls bending), t is time, $\Delta p$is the pitch of the lead screw M3 (0.5mm), and W_{m1} is the frequency of rotation of Motor 1. The relationship between time, t, frequency of rotation of Motor 1, W_{m1} ,and bending angle, θ, is given in Fig. 4 (c).

The setup for scanning a raster pattern over a portion of a spherical surface is presented in Fig. 4 (d). Thelength of the raster, L_t , achievable in a given time, t, is related to the angle of rotation for each loop, β_t, and the initial bending angle, θ_{start} , and the range of the bending angle, $\Delta\theta_t$, by (7):

$$L_t = \beta_t \cdot r \cdot \sin(\theta_{start} + \Delta\theta_t) \tag{7}$$

$$\beta_t = \frac{W_{m2} \cdot \pi}{\mu_2 \cdot 30} \cdot t \tag{8}$$

whereμ_2 is the gear reduction ratio of Motor 2 which controls rotation, r is the radius of the sphere, and W_{m2} is the frequency of rotation of Motor 2.

For cases where the lines of the raster don’t overlap, the approximate mosaic area is given by (9), being simply the product of length of the raster, L_t , and the diameter of the field-of-view of probe,Δh.

$$S_t = L_t \cdot \Delta h \tag{9}$$

The relationship between mosaic area, time and angular rotation for each loop is illustrated in Fig. 4 (e). Note that the initial bending angle is 45 degrees, the initial rotational angle is 0 degrees, the frequency of rotation of Motor 2 is 1000 rpm, and the frequency of rotation of Motor 1 (used for bending) is 3000 rpm.

The control diagram of the 1-DOF bending motion of the tip is shown in Fig. 4 (f). In Fig. 4 (f), $\theta_t$is the angle of Motor 1 driving the linkage,

$P(\theta_t)$ is the target linear displacement of the linkage, Y_t and Y_f are the target and current linear displacements of the linkage respectively, ΔY is the differential linear displacement of the linkage, and $S(\Delta Y)$ is the mapping function from displacement ΔY to output voltage, and V and θ_f are the output voltage and 1-DOF bending angle. The control process of the 1-DOF rotational motion is similar, but with rotational rather than linear displacement and using a Hall sensor to for closed loop control.

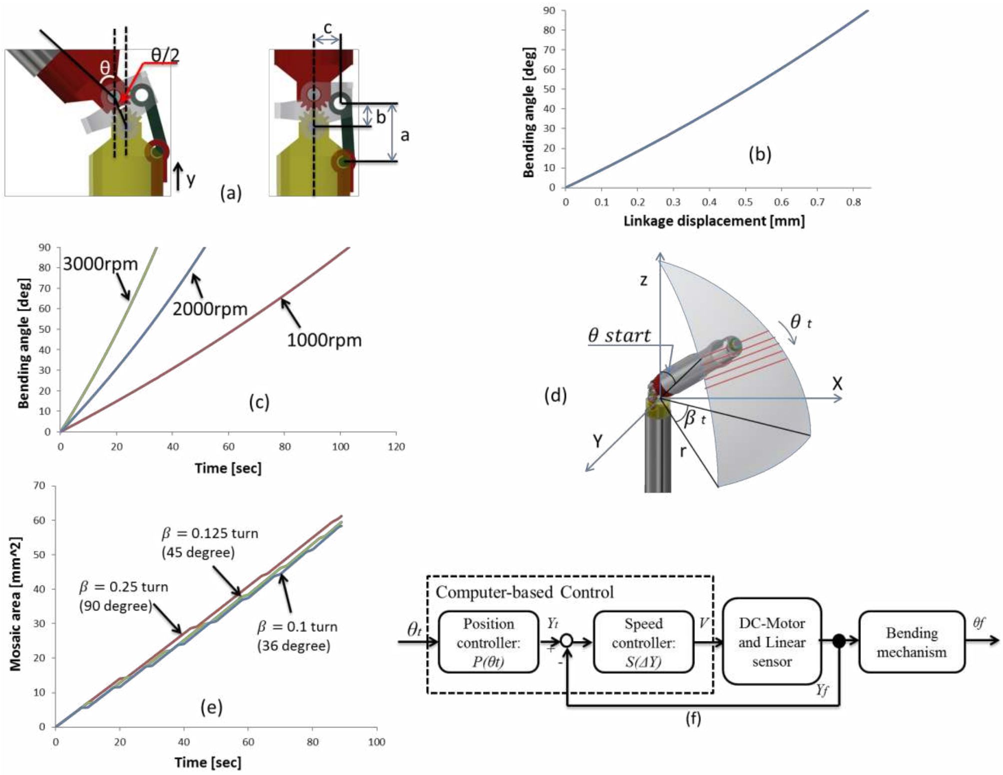

FIGURE 4. (a) Concept of 1 DOF bending mechanism. (b) Relationship between linkage displacement and bending angle. (c) Relationship between time and bending angle. (d) Co-ordinates for spherical raster. (e) The mosaic area that the device can scan over in a given time for values of angle of rotation, β_t,.(f) Control diagram for bending.

Visualisation and Mosaicing

The endomicroscope imaging probe was built in-house, using a leached fibre bundle containing 17,000 cores, each essentially providing a 'pixel' in the final image. As suggested previously [29], using a leached fibre bundle, which is much more flexible than the fused bundles typically used in endomicroscopy, enabled the use of full range of motion of the scanner. However, as discussed previously [29], the leached bundles have a large core-core spacing of 8 µm, which limits resolution. Therefore, we coupled a 2X, 0.8 NA magnification micro-lens (GT-MO-080-0415-488, GRINTech GmbH, Germany) to the distal end of the bundle, enhancing the resolution by a factor of 2 (Fig. 5(b)). The micro-lens and bundle are connected by epoxying inside a laser scintered concentric tube, which is fixed to the slider of the scanner by screws. The lens also increases the working distance from 0 to approximately 80 µm in air, which is important for allowing good quality confocal imaging through the approximately 20 µm thickness of the balloon.

The probe is coupled to a fluorescence confocal endomicroscope of an in-house design and based around a commercial laser scanning confocal system (CLS, Thorlabs USA). It operates at 488 nm wavelength and collects fluorescence emission above 500 nm by a photo-multiplier tube via a pinhole and a fluorescence filter set. A custom interface to an endomicroscope probe was built using a tube lens, a scan lens and a microscope objective, arranged so that a raster pattern was scanned over the distal end of a probe at 20 frames per second. Videos were recorded using the laser scanning unit's software and processed off-line. Each raw image was 800 x 800 pixels.

In the first stage of processing, the pattern of the fibre cores was removed and fluorescence background from the fibre bundle was removed using an approach similar to that reported in [18]. In brief, a background image was acquired with the probe not in contact with the tissue, and a calibration image was formed by averaging over 200 image frames while the probe was scanning. From the calibration image, the (x,y) pixel co-ordinate of the centre of each fibre core was found and the intensity of each core in the background ($I_{B,i}$) and calibration ($I_{C,i}$) images was extracted. A Delaunay triangulation was then formed over the core positions, allowing each pixel on a reconstruction grid to be associated with an enclosing triangle of three fibre cores (k, l, m), and its position recorded in barycentric co-ordinates with respect to the vertices of the triangle ($b_{i,k}$, $b_{i,l}$, $b_{i,m}$).

For each image in the video, the core intensities ($I_{raw,i}$) were then extracted by taking the pixel values at each previously calculated core location and then corrected for core-core variations and background signal using:

$$I_i = \frac{I_{raw,i} - I_{B,i}}{I_{C,i}}$$

To reconstruct each pixel on the reconstruction grid, a linear triangular interpolation was made between the corrected intensity values of the three surrounding cores, such that

$$I_{final,i} = I_k b_{i,k} + I_l b_{i,l} + I_m b_{i,m}$$

Finally, each image was cropped to a circle with a diameter of 480 pixels (equivalent to 330 microns on the tissue surface), and resized to 300 x 300 pixels by bicubic interpolation.

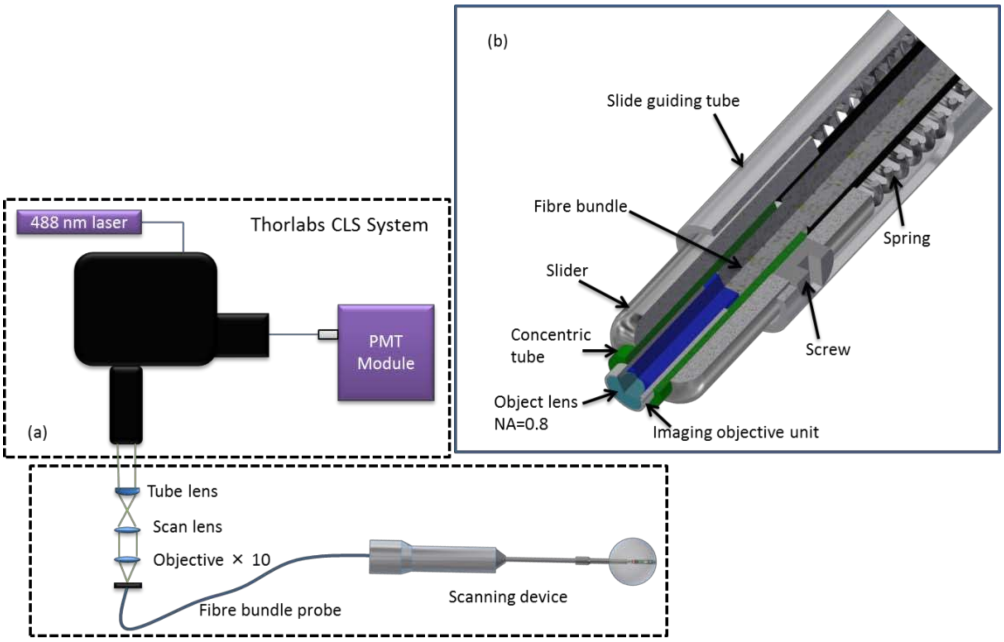

FIGURE 5.(a) Optical layout of laser scanning confocal endomicroscopy system, (b) Three quarter section view of distal end.

For mosaicing, the pair-wise normalised cross correlation was calculated between a template extracted from each image and the previous image. The position of the peak of the cross correlation was taken to be the shift between the two images. To create the mosaic, each image was inserted into the mosaic with the correct shift relative to the previous image using distance-weighted alpha blending to smooth the transition between frames.Correction of distortions due to probe tracking the balloon surfacemay be achieved using a more sophisticated mosaicing algorithm which does not assume rigid transformations [20]. These algorithms maybenot suitable for real time image reconstruction [31], but could be used for retrospective analysis. However, development of such algorithms is not the focus of this paper.

RESULTS

Mechanical Performance Evaluation

We evaluated bending and rotating characteristics of the 2-DOF scanning mechanism. These measurements were made with the imaging probe inserted into the channel. Repeatability measurements were performed over five trials, measuring actual bending and rotational angles against the target angles. For assessment of the bending performance, measurements were made in two parts: (a) bending from 0 degrees to 90 degrees, and (b) returning to 0 degrees. Backlash compensation was made by inverse rotation of Motor 1 when changing the bending direction. The bending angles were measured by a high-resolution digital camera set up over the tip. The accuracy of the camera image was checked by capturing a regular grid image (pitch 0.05 mm) before the experiments. No distortion was visible and, thus, the error caused by distortion was assumed to be negligible. The measured hysteresis curve is shown in Fig. 6(a), and the relationship between the target angle and bending repeatability error is given in Fig. 6(b). The measured values of bending range, bending repeatability error (standard deviation), and tip positioning accuracy are presented in Table I.

We also tested in detail the performance of the rotational motion. The scanning device was first rotated from 0 to 360 degrees (c), and then returned to 0 degrees (d) (Fig. 6(c - d) and Table II). Moreover, we tested the following capability of rotating motions between 0 and 360 degrees (Fig. 6(e)). The frequency of rotation of Motor 2 was 1000 rpm.

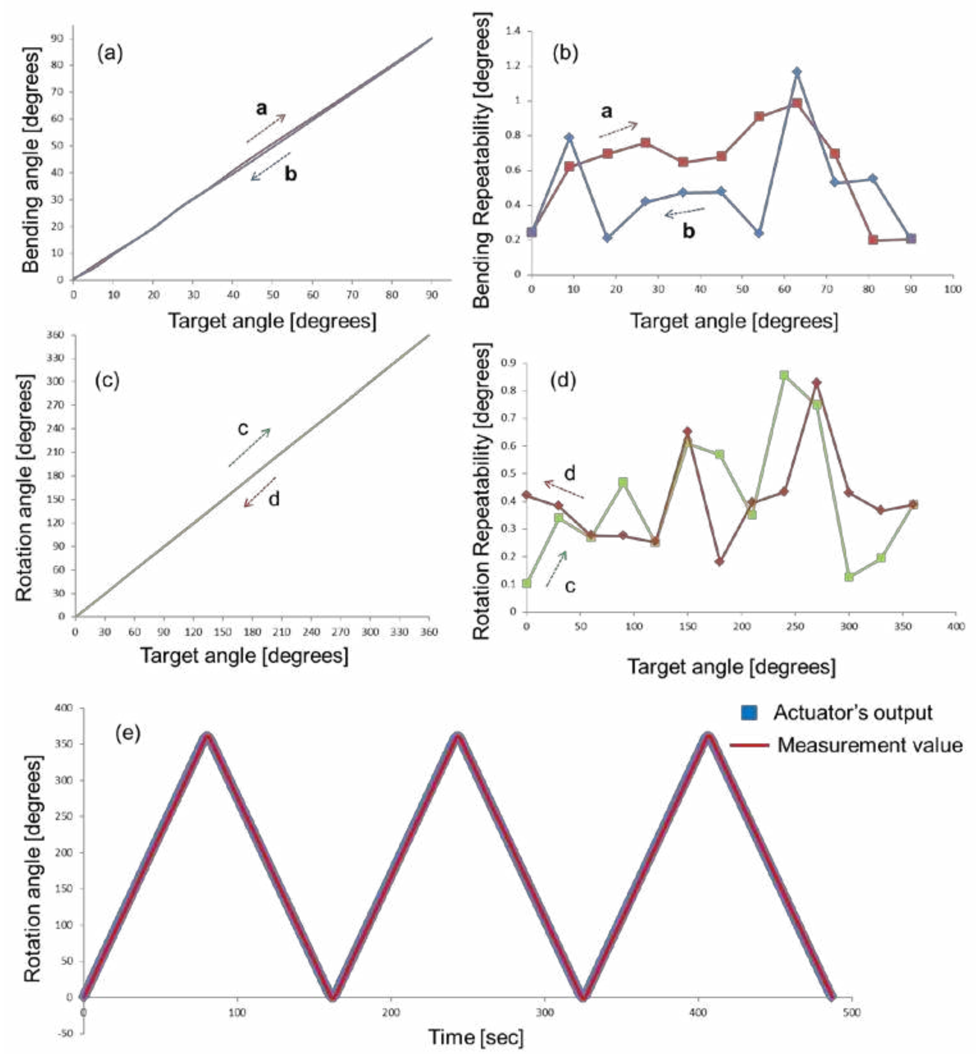

FIGURE6.Results of 2-DOFs scanning characteristics test, showing the relationship between target angles and actual bending and rotational angles. (a) 1-DOF target bending angle against measurement angle, (b) relationship between target bending angle and bending repeatability error, (c) 1-DOF target rotational angle against measurement angle, (d) relationship between target rotational angle and rotational repeatability error, (e) following capability of rotational motions between 0 and 360 degrees.

TABLE 1.Result of repeatability measurement in each bending mechanism.

Measurement item	(a)	(b)
Bending range (°)	0.26 to 90.10	90.10 to -0.692
Repeatability (°)	0.60	0.48
Tip positioning accuracy (mm)	0.26	0.2

TABLE 2. Result of repeatability measurement in rotating mechanism.

Measurement item	(c)	(d)
One circle rotational range (°)	0 to 359.96	359.96 to -0.36
Repeatability (°)	0.39	0.40
Tip positioning accuracy (mm)	0.17	0.17

TABLE 3.Generated power and torque at tip.

DOF	Direction (°)	Power [N]	Torque [Nmm]
Bending	0 to 90	0.6	15
Rotating (Bending 45°)	-360 to 360	1.6	40

Breast Phantom Experiment

For general performance evaluation, we simulated use of the system during breast conserving surgery using a silicon breast phantom as shown in Fig. 7(a). The breast phantom contained a realistic cavity as it had previously been used for surgical training for this procedure. To allow microscopic imaging, the cavity was lined with tissue paperstained with acriflavine.The scanning device wasattachedto a passive arm during experiment.

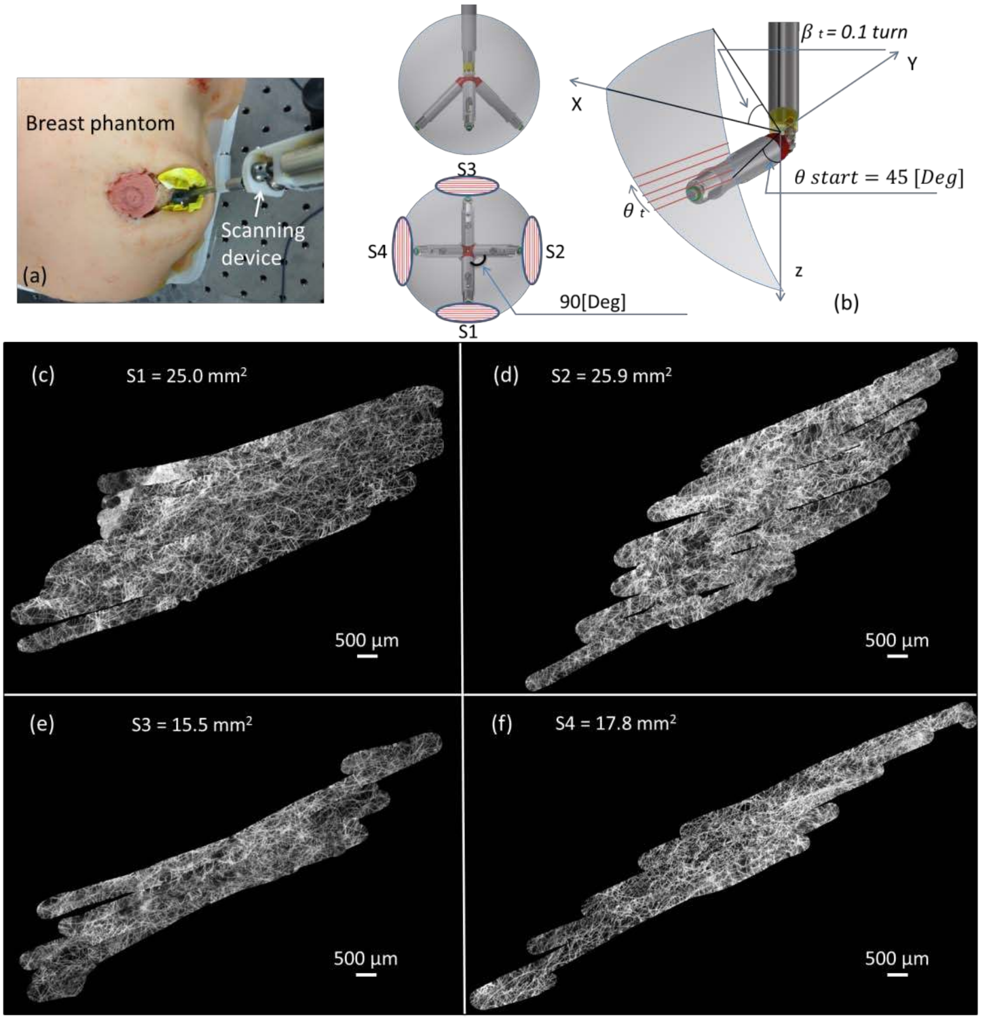

FIGURE 7. Breast phantom experiment results showing (a) the experimental set up: the cavity was lined with tissue paperstained with acriflavine. The scanning device was attached to a passive arm during experiment, (b) scanning position: four parts of the hemisphere (90 degrees apart) were targeted; the spacing between each line was set at 0.25 mm, and the angle of rotation for each loop at 0.1 turn which is 36 degrees, and (c-f) raster mosaics derived.

We performed raster scans using the rotational motion as the fast axis and the bending motion as the slow axis. The starting position and scanning area are shown in Fig. 7 (b). We scanned four parts of the hemisphere (90 degrees apart); the spacing between each line was set at 0.25 mm, and the angle of rotation for each loop at 0.1 turn which is 36 degrees (Fig. 7 (b)). Fig. 7(c-f) shows the four mosaics which cover an area of approximately 25.0 mm^2, 25.9 mm^2, 15.5 mm^2 and 17.8

mm^2. In Fig. 7(c-f), the intended automatic scan areas are 33.1 mm^2, 36.9 mm^2, 19.2 mm^2, and 21.3 mm^2 respectively. Thus, the ratio of the covered area to the intended area are 0.75(in Fig. 7 (c)), 0.7 (in Fig. 7 (d)), 0.8 (in Fig. 7 (e)), and 0.84 (in Fig. 7 (f)) respectively.

The results show that the probe could maintain almost constant tissue contact when scanning over large area on different parts of hemisphere surface. There was distortion in the mosaics, primarily due to deformation of the phantom during scanning. This deformation affects repeatability, and prevents scanning over an exactly defined area, but we were able to extract mosaics covering significant areas. This demonstrates that, in principle, large area imaging inside a realistic breast cavity phantom is possible. This result is also important because it demonstrates that the mechanism, including the inflated balloon, allows reshaping and scanning of irregular surfaces, as would be encountered in practice.

Ex vivo Human Breast Tissue Experiments

The above demonstrated a capability to image within a breast-cavity, but the imaging phantom was not representative of breast tissue. We therefore performed imaging studies using freshly excised, acriflavine-stained human breast tissues in order to confirm that large mosaics could be formed. The subject gave prior written informed consent and Human Tissue Authority licence and ethics approval was obtained through Imperial College Tissue Bank (No. CX803886). As only a small portion of tissue was available (approx. 20 x 10 mm), we placed this inside a hemispherical plastic shell (radius 30 mm) to provide an approximate simulation of the curvature of the breast cavity (Fig. 8(a)). We performed raster scans, with the spacing between raster lines set at 0.25mm(Fig. 8(b)).The scanning device was hold by passive arm during experiment.

Examples of mosaics extracted from these experiments are shown in (Fig. 8(c-e)). Fig 8(c-d) are for angle range of 36 degrees, while Fig 8(e) is for an angle range of 45 degrees. These images demonstrate that the key morphological features of normal breast tissue can be identified. Most prominent are the adipocytes, the large polygonal-shaped fat cells, while areas of fibrous tissue can also clearly be seen. When compared with the our previous results of scanning using a Gastroflex UHD Probe (Mauna Kea Technologues) [29], this provides indicates that the use of a highly flexible leached bundle probe, together with a distal micro-lens, could provide adequate image quality.

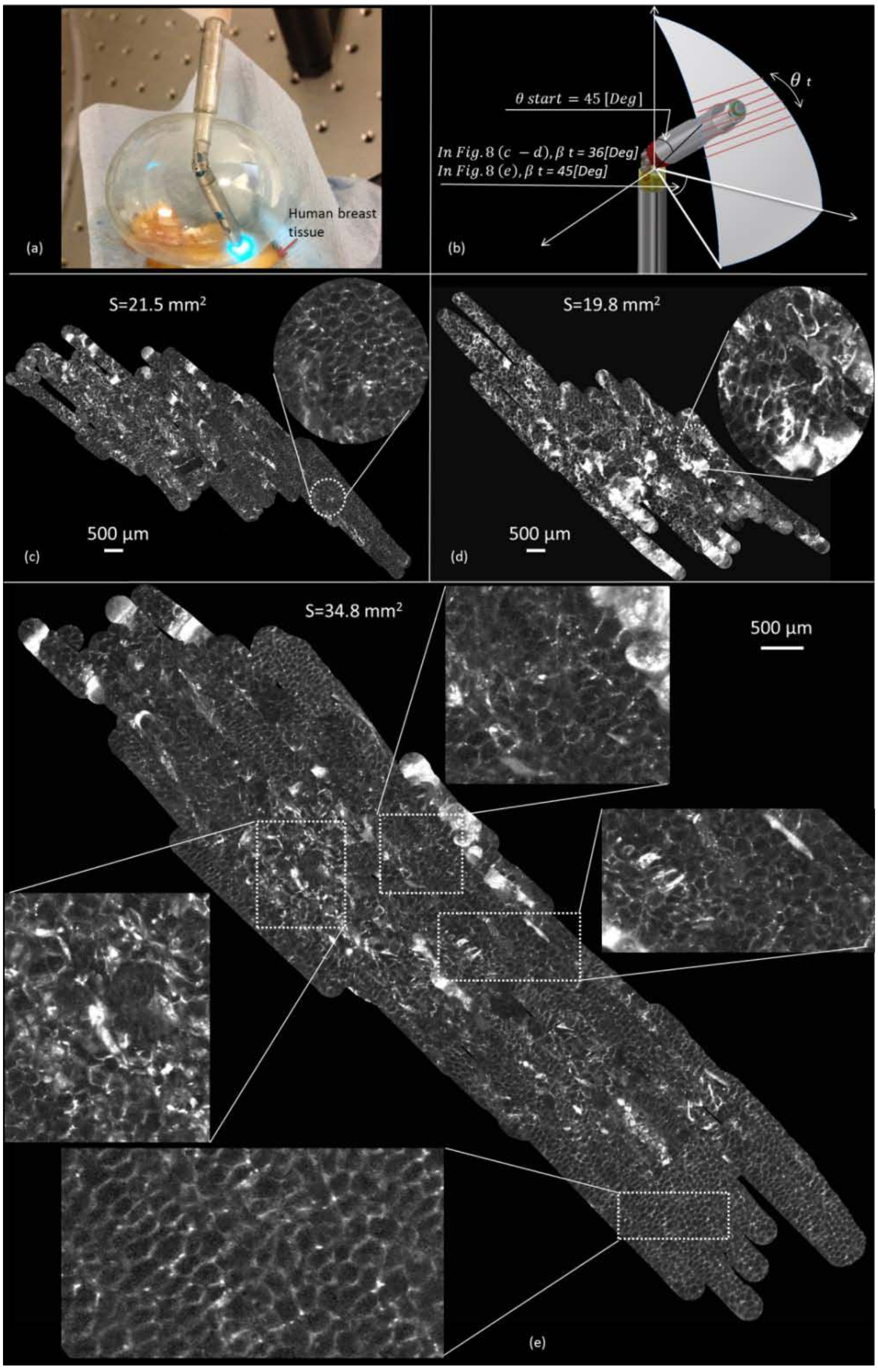

FIGURE8.Human breast tissue mosaic images, (a) Setup, (b) Scanning position, (c– e) Raster mosaic results of human breast tissue.

Fig. 8(c) shows a mosaic that covers an area of approximately 21.5 mm^2. The ratio of the covered area to the intended area (34.1 mm^2) is 0.63. Fig. 8 (d) shows a second scan, where the raster has an area approximately 19.8 mm^2. The extended area is 27.7 mm^2, resulting in an area ratio of 0.71. We observed that scan here is deformed and sheared; the main cause is likely to be movement of the specimen during scanning.

Finally, Fig. 8(e) is a mosaic covering an area 34.8 mm^{2}and the ratio of the covered area with respect to the intended area (38.69 mm^2) is 0.9.The very large image mosaics that could be generated allow for a much more global appreciation of the tissue morphology than can be achieved through individual images or small, manual mosaics.

DISCUSSION

In this paper, we have developed a miniature robot scanning probe for in vivo application of endomicroscopy for breast cancer surgery. By using the scanning device, we achievedmosaics approaching 35 mm^2 in size. Previous studies such as [22] were targeted towards generation a continuous mosaic of less than 3 mm^2, and so this device represents a significant increase in area coverage. Key novelties in this work include the incorporate of an inflatable balloon and design of an endomicroscope with sufficient flexibility to image anywhere on the hemisphere and with a working distance sufficient to image through the balloon.

It has been shown that the scanning device can achieve a repeatability of 0.6 degrees (bending motion) and 0.40 degrees (rotational motion). This corresponds to positional accuracies of 0.26 mm and 0.17 mm at the tip, respectively. This is comparable to the field-of-view of the endomicroscope probe (0.33 mm) and far smaller than any likely tissue deformation effects. Therefore in practice it may be necessary to over-sample to ensure complete tissue coverage.It is important to achieve speedy scanning, thus, we selected the maximum acceptable scanning velocity which could obtain consistent imaging mosacingby experiments. For example, it took almost 50 seconds to reach the targeted scanning area 30 mm^2 as shown in Fig. 4 (e). At present, the waiting time for other methods of examining tumor margins such as frozen section can be as long as 40 minutes. Intraoperative specimen x-rays may take as long as 5-10 minutes but it has low accuracy rates. The ability to obtain good imaging quality within a minute is certainly well for in vivo.

We used the device to scan raster patterns on a spherical surface, with the rotational motion used for the fast axis and the bending motion used for the slow axis. The achievable bending range was slightly over 90 degrees due to overrun of the linkage, but that doesn't affect the practical performance of the device. The bending and rotating forces were measured to be 0.6 N and 1.6 N respectively. This was evidently sufficient in order to carry out a scan inside the balloon.

The extension and deformation of the spur gear's engagement parts could be minimized by increasing the thickness of the spur gear. However, the backlash was small because the spur gears are used for guiding the bending motion instead of driving it. Moreover, backlash often occurs when changing the rotational direction of the gears; when forming the slow axis of a raster the motion was in a single direction only. Nevertheless, the quality of the connecting parts of the linkage could be improved in future. The positioning inaccuracies could be reduced by increasing the precision and stiffness of the gear and linkage. Because the inner air pressure is 140kPa which is a low pressure, the tissues will not be damaged even there is an air leakage. Using an aqueous to inflate the balloon is another option which has potential to provide better refractive index matching minimizing internal reflections.

Experiments with the realistic breasts phantom showed that, in principle, the probe can maintain contact with irregular surfaces. This is helped greatly by the inflatable balloon that tends to reshape the surface. The balloon could be moved due to reaction force exerted by tissue and probe. A passive linear structure is used to solve this issue.The passive linear structure with a working distance 3 mm, meaning that the hemispherical radius can vary by 3 mm at the tip which could cover a certain level of distance. We show that, thanks to the contact modulation effect of the passive linear structure and the reshaping effect of the balloon, the probe can maintain contact over large area during phantom experiment. We observed failures to image some parts of the phantom. It is therefore unlikely that an entire hemisphere could be imaged in a single shot, and the device would need to be positioned to as to optimize contact for a particular region of the cavity. Further work will be needed to explore the optimal workflow in this regard.It may also be necessary to optimize the size of the balloon and the length of the bending tip for different sized cavities. A range of differently sized balloons could be used to suit different cavities.For initial work, we targeted a 5 cm diameter cavity as; in general, a smaller cavity provides more challenges in terms of miniaturization and robustness.

In the *ex vivo* human tissue evaluation, the device was shown to be able to scan the tissue stably. These results demonstrate that when contact is maintained, the motion of the probe and the image quality are suitable for generating large area mosaics from breasts tissue. Except one very successful mosaics (Fig. 8(e)), the rate of area covered by the mosaic to the intended area in ex vivo experiments is smaller (0.63 and 0.71 in Fig. 8(c-d)) than those with the breast phantom mosaics performed in Fig 7 (average ratio is 0.77). There are two reasons. The first is that the breast phantom with tissue paper is less sticking and deformationthan human breast tissue. The second reason is the stabilizing effect of the balloon. The inflation of the balloon causes the tissue to deform and take on the shape of the inflated balloonthat provides for stabilization of the tissue. There will be tissue distortion caused by the inflated balloon and scanning probe. To an extent this problem is unavoidable, as any contact based imaging method will result in tissue deformation if the probe is driven across the tissue. Scanning the internal cavity surface directly with only the probe could lead to large tissue deformation and losing tissue contact since the excised tissue cavity is highly irregular. On the other hand, the distortion of the cavity surface by inflated balloon works as a “positive deformation” which could stabilize the irregular tissue cavity and limit uncontrollable tissue deformation. Further work will be needed to determine the effect of this on image interpretation. In future, this could include an automated balloon shaping mechanism using pressure control to allow a precise fit to the size of the cavity.Closed loop control of the device, using visual servoing based on position estimates from the image registration, is likely to be necessary in to progress further.

Our miniature balloon scanning device is a smart, cost-effective platform to generate accurate mosaics in real-time to aid intraoperative decision making. A particular benefit is the simple mechanical design, which will make commercial deployment feasible.

CONCLUSION

In this paper, we have presented and characterised a miniature scanning device for microscopic imaging of the walls of the cavity created during breast conserving surgery. Its novel features include a small diameter, a custom and highly flexible endomicroscopy probe to allow use of the full range of motion, an inflatable balloon to provide a more regular surface for imaging, and its ability to scan over a large surface area. We demonstrated the possibility of reshaping and scanning over irregular surfaces using a realistic breast cavity phantom, and the ability to form mosaics over breast morphology using *ex vivo*humantissue. The resulting mosaics show that the 2-DOF scanning approach, when combined with the inflatable balloon mechanism, allows imaging at high resolution over a large surface area. Despite the use of a balloon, deformation of the tissue remains a challenge and further research to tackle this problem will be needed if repeatability is to be improved. Nevertheless, these results demonstrate the potential clinical value of the device to improve the prospects for intraoperative cavity margin evaluation, which in future could lead to improved outcomes for breast cancer patients.

ACKNOWLEDGMENTS

The authors would like to thank Dr. Daniel R Leff and Vyas Khushi for providing the breast tissueand discussion for ex vivo experiments, and to Petros Giataganas for discussions with mechanical design. This work was supported by EPSRC grant EP/IO27769/1: SMART Endomicroscopy.

CONFLICT OF INTEREST

None.

REFERENCES

[1] Ferlay, J. et al. Cancer incidence and mortality worldwide: sources, methods and major patterns in GLOBOCAN 2012. Int. J. Cancer 136: E359–E386, 2015.

[2] Schwartz, G.F., U. Veronesi, K.B. Clough, et al. Consensus conference on breast conservation, J. Am. Coll. Surg. 203: 198-207, 2006.

[3] Singletary, S.E. Surgical margins in patients with early-stage breast cancer treated with breast conservation therapy, Am. J. Surg. 184: 383-393, 2002.

[4] Kreike, B., A. A. Hart, T. van de Velde, J. Borger, H. Peterse, E. Rutgers, H. Bartelink, and M. J. van de Vijver. Continuing risk of ipsilateral breast relapse after breast-conserving therapy at long-term follow-up, International journal of radiation oncology, biology, physics 71: 1014-1021, 2008.

[5] Xu M., L.V.Wang.Photoacoustic imaging in biomedicine. Rev SciInstrum 77:041101, 2006

[6] Jabbour, J. M., M. A. Saldua, J. N. Bixler. And K.C. Maitland. Confocal Endomicroscopy: Instrumentation and Medical Applications, Ann. Biomed. Eng. 40:378–397, 2011.

[7] Pohl, H, T. Rosch, M. Vieth, M. Koch, V. Becker, M. Anders, A.C. Khalifa, and A. Meining. Miniprobe confocal laser microscopy for the detection of invisible neoplasia in patients with Barrett's oesophagus. Gut 57:1648–1653, 2008.

[8] Newton, R.C., S.V. Kemp, G.Z. Yang, A. Darzi, M.N. Sheppard, and P.L. Shah. Tracheobronchial Amyloidosis and Confocal Endomicroscopy. Respiration 82(2):209–211, 2011.

[9] Newton, R.C., S. Kemp, Z. Zoumot, G.Z. Yang, A. Darzi, and P.L. Shah. An unusual case of haemoptysis. Thorax 65:309, 353, 2010.

[10] Newton, R.C., S.V. Kemp, G.Z. Yang, D. Ellson, A. Darzi, and P. Shah. Imaging parenchymal lung diseases with confocal endomicroscopy. Respiratory Medicine 106(1):127–137, 2012.

[11] Newton, R.C., S.V. Kemp, P. Shah, D. Elson, A. Darzi, K. Shibuya, S. Mulgrew, and G.Z. Yang. Progress toward optical biopsy:bringing the microscope to the patient. Lung 189:111–119, 2011.

[12] Gmitro, A. F., and D. Aziz. Confocal microscopy through a fiber-optic imaging bundle, Optics Letters, 18: 565-567, 1993.

[13] Le Goualher, G., A. Perchant, M. Genet, C. Cave, B. Viellerobe, F. Berier, B. Abrat, and N. Ayache. Towards optical biopsies with an integrated fibered confocal fluorescence microscope. Part II. In: Proceedings of the 7th International Conference on Medical Image Computing and Computer-Assisted Intervention, Saint-Malo, France, pp. 761–768, 2004.

[14] Laemmel, E., M. Genet, G. Le Goualher,Perchant A, J.F. Le Gargasson, and E. Vicaut, Fibered confocal fluorescence microscopy (Cell-viZio™) facilitates extended imaging in the field of microcirculation, Journal of Vascular Research 41(5): 400-411, 2004.

[15] Abeytunge, S., Y. Li, B. Larson, G. Peterson, E. Seltzer, R. Toledo-Crow, et al. Confocal microscopy with strip mosaicing for rapid imaging over large areas of excised tissue. Journal of biomedical optics 18: 061227, 2013.

[16] Chang, T. P., D. R. Leff, S. Shousha, D. J. Hadjiminas, R. Ramakrishnan, M. Gudi, R. Al-Mufti, M. R. Hughes, A. Darzi, and G. Z. Yang. Imaging of breast cancer morphology using probe-based confocal laser endomicroscopy: Towards a novel imaging tool for real-time intra-operative cavity scanning, Eur J SurgOncol. 39(11): S80, 2013.

[17] Tilli, M. T., M. C. Cabrera, A. R. Parrish,K.M. Torre, M.K. Sidawy, A.L. Gallagher, E. Makariou, S.A. Polin, M.C. Liu, and P.A. Furth. Real-time imaging and characterization of human breast tissue by reflectance confocal microscopy, Journal of biomedical optics. 12: 051901, 2007.

[18] Jeevan, R., D. Cromwell, M. Trivella, G. Lawrence, O. Kearins, J. Pereira, C. Sheppard, C.M. Caddy, J.H. van der Meulen. Reoperation rates after breast conserving surgery for breast cancer among women in England: retrospective study of hospital episode statistics," BMJ: British Medical Journal, 345, 2012.

[19] Vercauteren, T., A. Perchant, X. Pennec, and N. Ayache. Mosaicing of Confocal Microscopic In Vivo Soft Tissue Video Sequences. In: Medical Image Computing and Computer-Assisted Intervention—MICCAI 2005, pp. 753–760, 2005.

[20] Vercauteren, T., A. Perchant, G. Malandain, X. Pennec, and N. Ayache. Robust mosaicing with correction of motion distortions and tissue deformation for in vivo fibered microscopy. Medical Image Analysis 10(5): 673–692, 2006.

[21] Mahé, J., T. Vercauteren, B. Rosa, and J. Dauguet. A Viterbi approach to topology inference for large scale

endomicroscopyvideo mosaicing, In Medical Image Computing and Computer-Assisted Intervention–MICCAI 2013, pp. 404-411, 2005.

[22] Rosa, B., B. Herman, J. Szewczyk, B. Gayet, and G. Morel. Laparoscopic optical biopsies: in vivo robotized mosaicing with probe-based confocal endomicroscopy, in Proc. of IROS'2011, San Francisco, California, pp. 25-30, 2011.

[23] Erden, M. S., B. Rosa, N. Boularot, B. Gayet, G. Morel, and J. Szewczyk. Conic-Spiraleur: A Miniature Distal Scanner for Confocal Microlaparoscope, IEEE/ASME transactions on mechatronics 19(6): 1786-1798, 2014

[24] Dario, P., M. Carrozza, C. Marcacci, M. Attanasio, B. Magnami, O. Tonet, and G. Megali. A Novel Mechatronic Tool for Computer-Assisted Arthroscopy," IEEE Trans. Inform. Technol. Biomed. 4(1): 15–28, 2000.

[25] Zuo, S., K. Iijima, T. Tokumiya, and K. Masamune. Variable stiffness outer sheath with "Dragon skin" structure and negative pneumatic shape-locking", International Journal of Computer Assisted Radiology and Surgery9(5): 857-865**,** 2014

[26] Shang, J., D. Noonan, C. Payne, J. Clark, M. Sodergren, A. Darzi, and G.Z. Yang. An articulated universal joint based flexibleaccess robot for minimally invasive surgery, Proc. IEEE Int. Conf. Robotics Automation, pp. 1147–1152, 2011.

[27] Peirs, J., D. Reynaerts, H. Van Brussel. A miniature manipulator for integration in a self-propelling endoscope, Sensors and Actuators A.: 343–349, 2001

[28] Yamashita, H., D. Kim, N. Hata, T. Dohi. Multi-slider linkage mechanism for endoscopic forceps manipulator, Proc. IEEE/RSJ Int. Conf. Intell. Robots Syst., pp. 2577-2582, 2003.

[29] Yamashita, H., K. Matsumiya, K. Masamune, H. Liao, T. Chiba, T. Dohi. Miniature bending manipulator for fetoscopic intrauterine laser therapy in twin-to-twin transfusion syndrome. Surgical Endoscopy 22(2): 430–435,2007

[30] Zuo, S., M. Hughes, C. Seneci, T.P. Chang, G.Z. Yang. Towards Intraoperative Breast Endomicroscopy with a Novel Surface Scanning Device, *IEEE Trans. Biomed. Eng.*, doi:10.1109/TBME.2015.2455597, 2015

[31] Vercauteren, T., A. Meining, F. Lacombe, A. Perchant, "Real time autonomous video image registration for endomicroscopy: fighting the compromises," In *Biomedical Optics (BiOS) 2008*, pp. 68610C-68610C, 2008.